Spaceborne bi- and multistatic SAR: potential and challenges

G. Krieger and A. Moreira

Abstract: Bi- and multistatic synthetic aperture radar (SAR) operates with distinct transmit and receive antennas that are mounted on separate platforms. Such a spatial separation has several operational advantages, which will increase the capability, reliability and flexibility of future SAR missions. Various spaceborne bi- and multistatic SAR configurations are introduced, and their potential for different applications such as frequent monitoring, wide-swath imaging, scene classification, single pass cross-track interferometry and resolution enhancement is compared. Furthermore, some major challenges such as phase and time synchronisation, bi- and multistatic SAR processing, satellite orbit selection and relative position sensing are addressed.

1 Introduction

Bistatic radar is defined as a radar where the transmitter and receiver are spatially separated [1]. In some definitions, it is also assumed that this spatial separation has to be a 'considerable distance' that is 'comparable' [2] or 'a significant fraction' [3] of either the target–receiver or the target–transmitter distance, but we will not limit our discussion to such systems with large baselines; our only assumption is that the transmit and receive antennas are on different platforms. Bistatic radar is not a new concept and its fundamental principles have been known and demonstrated many years before the development of an operational monostatic radar [4]. However, the interest in bistatic radar dropped quickly after the invention and demonstration of the monostatic radar principle in the late 1930s. The major reason for this decline was the desire of many users to have a radar operated from a single site. Since then bistatic radars have been 'rediscovered' several times, mainly for military applications such as receiver camouflage and precise target location, and to counter stealth. Only recently, bistatic radar also received increasing interest with respect to synthetic aperture radar (SAR) and a number of spaceborne bi- and multistatic radar missions have been suggested, some of which are now under development or in planning [5–17]. The suggested systems may be divided into fully and semi-active configurations. In a fully active configuration, each radar has both transmit and receive capabilities as illustrated in Fig. 1 on the left. Examples for fully active systems are the multistatic TechSAT 21 constellation [8] and the bistatic TerraSAR-X tandem [17]. Semi-active systems combine an active illuminator with one or more passive receivers as shown in Fig. 1 on the right. Examples for semi-active systems are the interferometric cartwheel [10] and BISSAT [11]. In principle, it is also possible to use the scattered signals from communication or navigation satellites for dedicated applications such as coarse scale differential interferometry [18], passive coherent location [19], air target detection [20], ocean altimetry [21] and sea state and wind retrieval [22].

The distributed functionality in bi- and multistatic SAR allows for a natural separation of the radar payloads and will therefore strongly support the use of small, low-cost satellites in the future. For example, deployable antennas and reduced power demands of passive receivers enable an accommodation of the radar payload on micro-satellites. Satellite constellations will allow for a modular design where the reuse of major building blocks shortens development time, increases reliability and reduces costs. The ultimate goal is a highly reconfigurable and scalable satellite constellation for a broad spectrum of remote-sensing applications [8, 23, 24]. Such a multi purpose system offers a flexible imaging geometry that may be dynamically adapted to different operational tasks.

2 Frequent monitoring

Most users require instant access to up-to-date SAR data. The revisit times of current spaceborne SAR sensors, ranging from several days to several weeks, will not suffice for important applications such as sea–ice monitoring and maritime services, risk and disaster management, traffic observation and security [25–29]. Distributed satellite constellations have the potential to shorten the revisit time substantially. One promising approach uses multiple passive-receiver satellites in conjunction with a geostationary illuminator (cf. Fig. 2) [30–33]. This concept allows for a systematic reduction of the revisit times as well as an upgrade to other imaging modes such as cross-track interferometry (cf. Section 4) and multiple aperture sensing (cf. Section 5) by increasing only the number of low-cost, passive receivers. Multiple missions may also share one or a small number of common illuminators, thereby reducing the costs of each individual mission significantly.

In order to analyse the feasibility of such a bistatic system with large transmitter–receiver separation, we will now investigate its performance. As the following analysis takes full account of the bistatic imaging geometry, it is also applicable to other bistatic SAR constellations, such as a global earth observation system for continuous

IEE Proceedings online no. 20045111

doi:10.1049/ip-rsn:20045111

Paper first received 14th October 2004 and in revised form 8th July 2005

The authors are with the Microwaves and Radar Institute, German Aerospace Centre (DLR), Oberpfaffenhofen, Germany

E-mail: gerhard.krieger@dlr.de

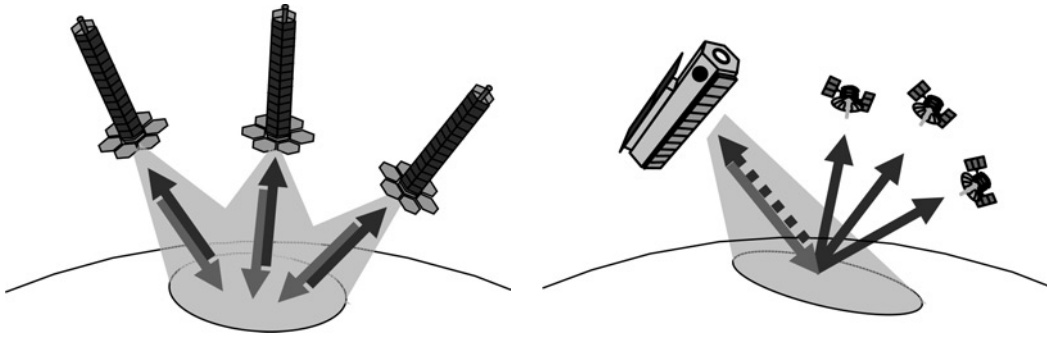

Fig. 1 *Fully active (left) and semi-active (right) multistatic radar systems*

monitoring based on multiple medium earth orbit (MEO) satellites. Table 1 summarises the major parameters of the exemplary bistatic SAR system, which serves as a reference for the following calculations.

For convenience, all computations will be performed in a local plane (x, y) that is tangent to the Earth's surface at the receiver nadir. The errors introduced by this approximation may be neglected for small receiver altitudes and it would be straightforward to extend the results to a spherical or elliptical geometry for receivers in higher orbits.

We start with a closer look at the resolution cell of the bistatic SAR. Fig. 3 shows the contours with constant range and Doppler in the tangent plane (x, y) for a receiver at 50° northern latitude and the same longitude as the geostationary transmitter. The circle in the centre denotes the receiver nadir and the arrow indicates the receiver velocity vector. As there is a priori no obvious range direction in a bistatic SAR, we define the range resolution vector field in the tangent plane (x, y)

$$\vec{\boldsymbol{r}}_{\mathrm{g}}(x,y) = \frac{\mathrm{grad}[r(x,y)]}{\|\mathrm{grad}[r(x,y)]\|^2} \cdot \frac{c_0}{B_{\mathrm{r}}} \tag{1}$$

where $r(x, y) = r_{\mathrm{Tx}}(x, y) + r_{\mathrm{Rx}}(x, y)$ is the sum of the transmit and receive path for each point (x, y) in the tangent plane, c_0 the speed of light and B_{r} the bandwidth of the transmitted signal. Note that for each position in the tangent plane, the vector $\vec{\boldsymbol{r}}_{\mathrm{g}}$ points always in the direction of the best range resolution (as is true for the ground range in a monostatic SAR) and its magnitude indicates the achievable ground range resolution. In a similar manner, we may derive the Doppler resolution vector

$$\vec{\boldsymbol{a}}_{\mathrm{g}}(x,y) = \frac{\mathrm{grad}[\,f_{\mathrm{Dop}}(x,y)]}{\|\mathrm{grad}[\,f_{\mathrm{Dop}}(x,y)]\|^2} \cdot \frac{1}{T_{\mathrm{int}}(x,y)} \tag{2}$$

Fig. 2 *Bistatic SAR consisting of a geostationary illuminator with LEO receivers*

where T_{int} denotes the receiver's coherent integration time and

$$f_{\mathrm{Dop}} = \frac{1}{\lambda}\left[\frac{\partial}{\partial t}(r_{\mathrm{Tx}} + r_{\mathrm{Rx}})\right] = -\frac{1}{\lambda}\left[\frac{\partial r_{\mathrm{Tx}}}{\partial t} + \frac{\partial r_{\mathrm{Rx}}}{\partial t}\right] \tag{3}$$

is the Doppler frequency of the bistatic SAR. Note that for the present geostationary system $\partial r_{\mathrm{Tx}}/\partial t = 0$, which will reduce the Doppler frequency and increase the signal-to-noise ratio (SNR) by a factor of 2 when compared with a monostatic SAR (the reduced Doppler frequency may also be of interest in ground moving target indication (GMTI) to improve clutter suppression). On the basis of the previous definitions, we may derive the area of a bistatic resolution cell (cf. Fig. 3, right) as

$$A_{\mathrm{rescell}} = \frac{\|\vec{\boldsymbol{r}}_{\mathrm{g}}\| \cdot \|\vec{\boldsymbol{a}}_{\mathrm{g}}\|}{\sin(\varphi)} = \frac{\|\vec{\boldsymbol{r}}_{\mathrm{g}}\|^2 \cdot \|\vec{\boldsymbol{a}}_{\mathrm{g}}\|^2}{\|\vec{\boldsymbol{r}}_{\mathrm{g}} \times \vec{\boldsymbol{a}}_{\mathrm{g}}\|} \tag{4}$$

where φ is the angle between the range and azimuth resolution vectors $\vec{\boldsymbol{r}}_{\mathrm{g}}$ and $\vec{\boldsymbol{a}}_{\mathrm{g}}$. For a calculation of the sensitivity of the system, we start from the bistatic radar equation (cf. Willis [1])

$$\mathrm{SNR} = \frac{P_{\mathrm{t}} G_{\mathrm{Tx}}}{4\pi r_{\mathrm{Tx}}^2} \cdot A_{\mathrm{rescell}} \sigma_B^0 \cdot \frac{A_{\mathrm{Rx}}}{4\pi r_{\mathrm{Rx}}^2} \cdot \frac{1}{kT_{\mathrm{s}} F B_{\mathrm{n}} L} \tag{5}$$

where P_{t} is the transmit power, G_{Tx} the gain of the transmitting antenna, A_{rescell} the size of the resolution cell for one look, A_{Rx} the effective aperture of the receive antenna, r_{Tx} the slant range distance from the transmitter to the imaged scene, r_{Rx} the slant range distance from the receiver to the imaged scene, k the Boltzmann constant, T_{s} the system noise temperature, F the receiver noise figure, B_{n} the noise bandwidth of the receiver and L the loss factor.

Table 1: Parameters of bistatic SAR with geostationary illuminator and low earth orbit (LEO) receivers

Wavelength	λ	3.1 cm (X-band)
Maximum bandwidth	B_{r}	300 MHz
Average transmit power	P_{avg}	1000 W
Antenna size Tx	A_{Tx}	100 m^2
Antenna size Rx	A_{Rx}	6 m^2
Noise figure + losses	$F + L$	5 dB
Transmitter altitude	h_{Tx}	35 850 km (geostationary)
Receiver altitude	h_{Rx}	400 km
Inclination (receiver orbit)	i	50°
Ground range resolution	Δrg	3 m
Azimuth resolution	Δaz	3 m
Coherent integration time	T_{int}	~0.5–1 s (variable)

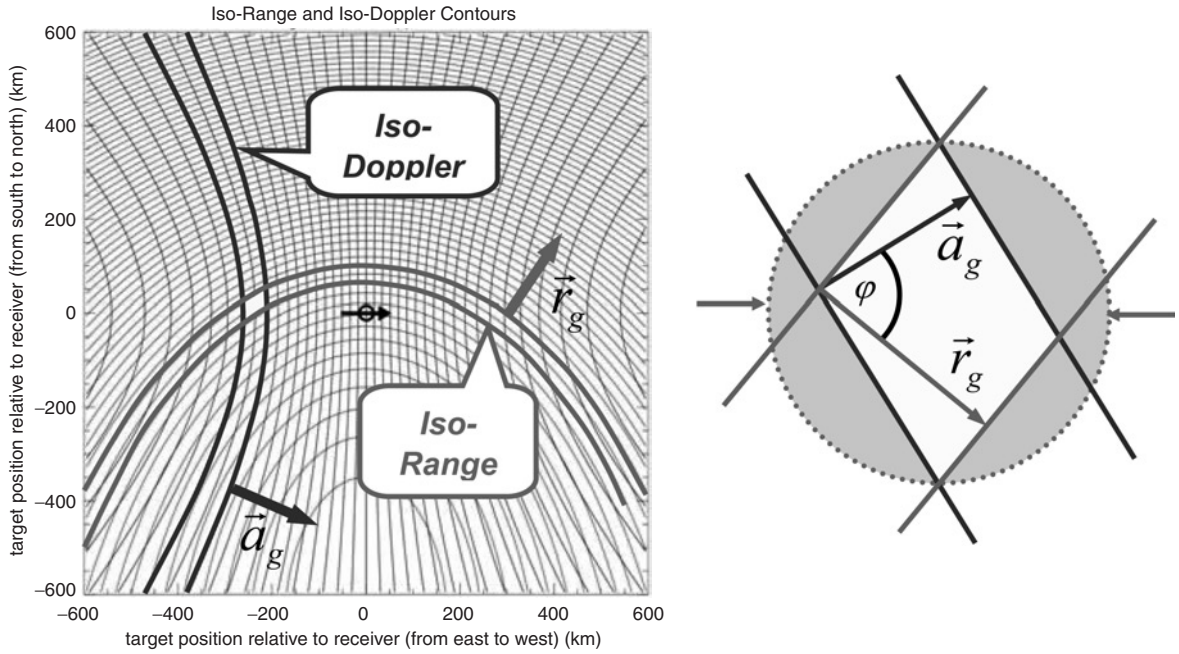

Fig. 3 *Iso-range (grey) and iso-Doppler (black) contours (left) and resolution cell (right), where $\vec{r}_g$ is the range resolution vector in the tangent plane and $\vec{a}_g$ is the Doppler resolution vector*

Bistatic SAR processing will now integrate multiple radar pulses of bandwidth B_n and pulse duration τ_p, thereby improving the SNR by a factor of $n_{rg} \cdot n_{az}$, where $n_{rg} = B_n \cdot \tau_p$ and $n_{az} = \mathrm{PRF} \cdot T_{int}$ are the number of independent data samples in range and azimuth, respectively. This implicitly assumes a match between the transmitted pulse bandwidth and the receiver filter ($B_n \simeq B_r$), a sufficient sampling frequency for unambiguous signal representation and a constant azimuth antenna pattern during the synthetic aperture time T_{int}. As the noise equivalent sigma zero (NESZ) corresponds to the radar scattering coefficient σ^0_B for which the SNR is equal to 1 (SNR = 0 dB), after a simple transformation, we obtain

$$\mathrm{NESZ} = \frac{(4\pi)^2 r_{Tx}^2 r_{Rx}^2 kT_s FL}{P_{avg} G_{Tx} A_{Rx} A_{rescell} T_{int}} \tag{6}$$

where $P_{avg} = P_t \cdot \mathrm{PRF} \cdot \tau_p$ is the average transmit power. Fig. 4 shows the NESZ for three different receiver locations. The NESZ computation is based on a fixed ground range resolution of 3 m, which requires a position-dependent range bandwidth B_r (e.g. 125 MHz at receiver nadir with $\theta_{Rx} = 0^\circ$ and $\theta_{Tx} \simeq 50^\circ$). As the bandwidth may not exceed an upper limit of 300 MHz because of current international frequency regulations in X-band, we have restricted the NESZ computation to those areas where $B_r < 300$ MHz. In Fig. 4, we have further assumed that the diameter of the resolution cell $d_{rescell}$, which is shown as dotted in Fig. 3 on the right, does not exceed a predefined limit of 6 m for a range and azimuth resolution of 3 m. The resolution cell diameter can be derived from the range and azimuth resolution vectors by

$$d_{rescell} = \frac{\sqrt{\|\vec{r}_g\|^2 + \|\vec{a}_g\|^2 + 2 \cdot \|\vec{r}_g\| \cdot \|\vec{a}_g\| \cdot |\cos(\varphi)|}}{|\sin(\varphi)|} \tag{7}$$

It becomes clear from Fig. 4 that it is possible to achieve an NESZ of less than -19 dB m^2/m^2 for a transmit power aperture product of 10^5 W m^2 (cf. Table 1) in the neighbourhood of the receiver nadir. This proves the physical feasibility of a distributed frequent monitoring SAR consisting

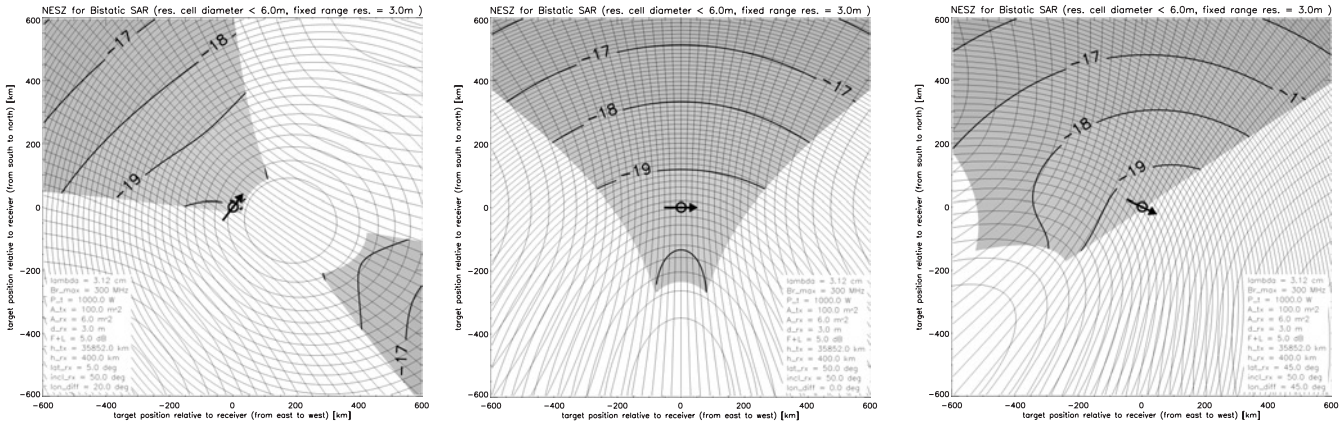

Fig. 4 *NESZ in tangential plane for receiver satellites at different longitudes and latitudes*

Latitudes of the receiver are 5° (left), 50° (middle) and 45° (right) and longitude differences between transmitter and receiver are 20° (left), 0° (middle) and 45° (right). The shaded areas in each plot indicate different NESZ levels for a ground range and azimuth resolution of 3 m subject to the constraint that the resolution cell diameter does not exceed 6 m

of a geosynchronous illuminator and multiple passive receivers in low Earth orbit without an unreasonable amount of resources. Note that such a system may also take advantage of forward scattering (cf. Section 3), which will increase the SNR, thereby reducing the requirements on both the transmit power and antenna size. The coverage region of a geostationary illuminator is limited to approximately $\pm 55^\circ$ latitude because of the shallow incident angles of the transmitted wave. This restriction may be avoided by using satellites in geosynchronous, medium Earth or Molniya orbits.

3 Bistatic observation

Bistatic SAR imaging provides additional observables for the extraction of important scene and target parameters (Fig. 5). Bistatic data may furthermore be combined with monostatic data to obtain a highly informative set of multiangle observations. A system dedicated to the simultaneous acquisition of mono- and bistatic SAR images has been suggested in Moccia *et al.* [34] together with a wealth of scientific applications. For example, a quantitative evaluation of the bistatic radar cross-section (RCS) facilitates the detection and recognition of targets based on their characteristic bistatic radar signatures [35–38]. Object detection in heterogeneous environments will furthermore take advantage of reduced retro-reflector effects as, for example, observed in bistatic SAR images of urban areas [39]. The segmentation and classification of natural surface and volume scatterers are alleviated by comparing the spatial statistics of mono- and bistatic scattering coefficients. Significant differences between monostatic and bistatic images have been observed in a bistatic SAR experiment even in the case of small bistatic angles [40], thus indicating that the monostatic–bistatic equivalence theorem [41] does not fully apply in this case. The information space may further be enhanced by fully polarimetric data acquisitions that are well suited to estimate important bio- and geophysical parameters of the Earth's surface and its vegetation cover. Peculiar effects may occur for bistatic out-of-plane scattering where the azimuth angle, as shown in Fig. 5, becomes different from $\phi = 0^\circ$. For example, the fully polarimetric measurements in Ulaby *et al.* [42], Mauck *et al.* [43] and Nashashibi [44] demonstrate that the cross-polarised HV scattering approaches or even exceeds the co-polarised HH and VV scattering for out-of-plane angles of $\phi \simeq \pm 90^\circ$. This polarisation twisting is, in part, a result of the bistatic out-of-plane geometry and its associated definition of the polarisation base [45]. The intricate dependency of the bistatic response on the azimuth angle has furthermore several implications for the design of fully polarimetric bistatic SAR systems and for the correct application of model-based parameter retrieval algorithms as used in, for example, polarimetric SAR interferometry (cf. Section 4).

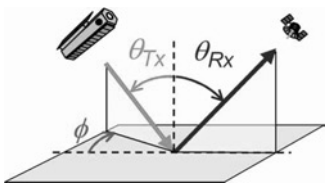

Fig. 5 *Extended observation space in bistatic radar (adapted from Simpson [145])*

θ_{Tx} is the incident angle, θ_{Rx} is the scattering angle and ϕ is the azimuthal out-of-plane angle

Further potential arises from evaluating the signals in a forward scattering geometry. For example, an increase in the bistatic in-plane scattering coefficient ($\phi = 0^\circ$) from -23 to $+6$ dB has been reported in Domville [46] for rural land in X-band. Similar results have been obtained in Sarabandi and Zahn [47] for rough metallic surfaces. The increased bistatic scattering coefficient can be used to enhance the radiometric sensitivity of a bistatic radar, but the reduced range resolution in a forward scattering geometry requires careful system design (cf. Section 2). Bistatic observations may also increase the RCS of manmade objects and/or the sensitivity to specific scattering centres of object composites [1, 43, 48], and bistatic polarimetry is well suited to improve the detection of objects embedded in clutter [49]. Further potential arises for glint reduction [1], which supports, together with the enhanced signal-to-clutter ratio, future applications such as wide area traffic monitoring from spaceborne satellite constellations. Moreover, the combined evaluation of mono- and bistatic range and Doppler enables precise target localisation and velocity measurements [1, 34, 50].

Bistatic observations in a forward scattering geometry have also great potential for systematic vegetation monitoring. For example, simulations of a forest model consisting of two layers over a rough surface indicate that an appropriately chosen bistatic imaging geometry is well suited to increase the sensitivity to individual scattering mechanisms, thereby alleviating an estimate of the canopy type and other forest parameters [51]. Forest biomass monitoring will take advantage of the specular coherent reflection from the soil, which enables more sensitive biomass estimates over a wider dynamic range with lower saturation when compared with a monostatic radar [52]. Specular reflection measurements are also suited for the retrieval of the soil dielectric constant [53, 54], but it is clear that the observation geometry has to be chosen with care: on one hand, a strong specular response will be desired for applications such as biomass and soil moisture retrieval, and on the other, the range resolution will become very poor, as the scattering angle θ_{Rx} approaches the incident angle θ_{Tx} in the case of in-plane forward scattering. Further challenges arise from range ambiguities in a pure forward scattering geometry. Such ambiguities could, in principle, be resolved by elevation null steering in a multiaperture configuration as outlined in Section 5.

Bistatic SAR is also of great advantage for oceanographic applications [55–59]. Examples are estimates of bistatic ocean wave spectra and the accurate retrieval of wind speed and sea state parameters. Several investigations show furthermore that the width and strength of the glistening (specular coherent) beam depend on the surface roughness [60–63]. Systematic acquisitions of bistatic scattering coefficients in a bi- or multistatic SAR may hence be used to measure surface roughness. Further potential arises for the estimation of terrain slope, stereogrammetric measurements, as well as meteorological and atmospheric applications [1, 11, 34, 64].

4 Single-pass interferometry

SAR interferometry is a powerful and well-established remote-sensing technique for the quantitative measurement of important bio- and geophysical parameters of the Earth's surface [65–70]. However, conventional repeat-pass interferometry suffers from temporal decorrelation and atmospheric distortions. Such limitations may be avoided by using a bi- or multistatic radar, which offers a natural way

to implement single-pass interferometry in space. A satellite formation enables a flexible imaging geometry with large baselines, thereby increasing significantly the interferometric performance for applications such as digital elevation model (DEM) generation in comparison to a single platform system, such as the Shuttle Radar Topography Mission (SRTM), that has to rely on a short baseline with fixed length. Single pass interferometry may be implemented either by a semi-active (Fig. 1, right) [10, 12, 15] or by a fully active (Fig. 1, left) [8, 9, 17] satellite constellation. Fully active systems have, in general, a higher sensitivity and flexibility, are less prone to ambiguities and enable easier phase synchronisation like in a ping-pong mode with alternating transmitters or by a direct exchange of radar pulses. Furthermore, they also provide a pursuit monostatic mode as a natural fallback solution in the case of problems with orbit control or instrument synchronisation. In contrast, semi-active radar constellations have a significant cost-advantage and will therefore provide more interferometric baselines per money. Several satellite formations have been suggested to provide an almost constant interferometric baseline across the whole orbit [10, 12]. Alternatives are constellations with multiple baselines at a fixed baseline ratio [15, 71]. The latter approach will substantially alleviate the problem of phase-ambiguity resolution in the case of large baselines, but a latitude-based acquisition strategy has to be applied to achieve global coverage [71, 72]. One example for such a formation is the Trinodal Pendulum, which is shown in Fig. 6 on the left.

The performance of this multibaseline, single-pass SAR interferometer has been investigated in a detailed ESA study, assuming an illumination by the planned TerraSAR-L satellite [15, 72]. The right-hand side of Fig. 6 shows the predicted height accuracy for a height of ambiguity of 100 m (dashed, corresponding to an effective interferometric baseline of $B_\perp \sim 1$ km) and 10 m (solid, corresponding to $B_\perp \sim 10$ km), assuming an independent post-spacing of 12×12 m^2. It is obvious that the height accuracy increases with a decreasing height of ambiguity. However, a small height of ambiguity is likely to cause phase-wrapping problems, especially in mountainous areas [73].

The baseline ratio of the example in Fig. 6 has been chosen such that the height errors from the DEM acquisition with the small baseline stay below the height of ambiguity for the large baseline. It would hence be possible to use the interferometric data from the small baseline acquisition to resolve phase ambiguities in the highly sensitive large baseline interferogram [74–78]. Large bandwidth interferometric systems may additionally apply the split spectrum approach to determine the absolute interferometric phase [79, 80]. Note that the simultaneous availability of multiple baselines with different lengths reduces significantly the phase-ambiguity gap between the large baseline interferogram and the synthetic, low-frequency interferograms [81]. By this, it becomes possible to push the DEM performance up to the limits of the critical baseline, which will enable powerful SAR interferometers for the generation of high resolution digital elevation models with a vertical accuracy below 1 m. It has been shown in Zink and Krieger [15] and Krieger and Fiedler [72], that a global DEM according to the emerging HRTI (high resolution terrain information) level-3 standard could be derived with the Trinodal Pendulum and TerraSAR-L in less than $1\frac{1}{2}$ years, assuming dual mapping with ascending and descending orbits and a mean monitoring time of 180 s per orbit. The combination of interferograms from ascending and descending orbits is well suited to solve residual problems in DEM generation arising, for example, from shadow in alpine terrain [78]. Multiple interferograms with different incident angles could also be acquired in a single pass by augmenting the multistatic configuration of Fig. 6 with additional receiver satellites.

A limiting factor for high resolution cross-track interferometry is volume decorrelation in vegetated areas. Volume decorrelation may become the dominant error source for large baseline acquisitions in the case of strong wave penetration into the volume. A possible solution to this problem is polarimetric SAR interferometry (PolInSAR),

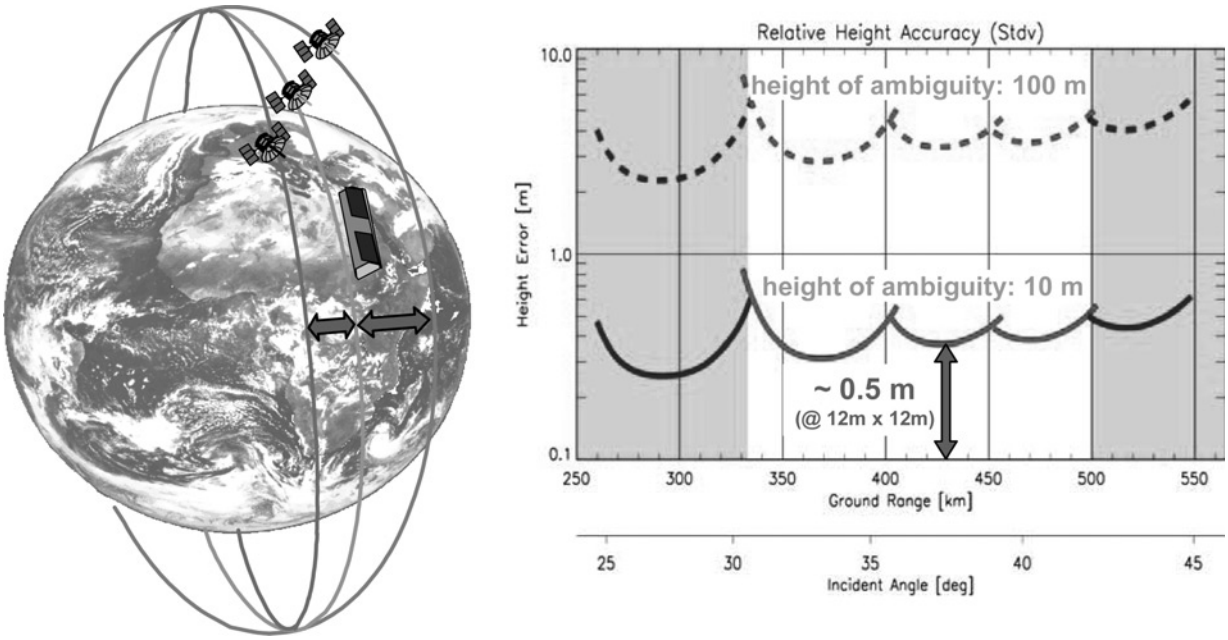

Fig. 6 *Multibaseline single-pass cross-track interferometry with the Trinodal Pendulum*

Left Orbit configuration with one illuminator and three passive receivers
Right Predicted DEM performance in combination with the planned TerraSAR-L satellite
The estimated height accuracy is shown for two baselines with a height of ambiguity of 100 m (dashed) and 10 m (solid)

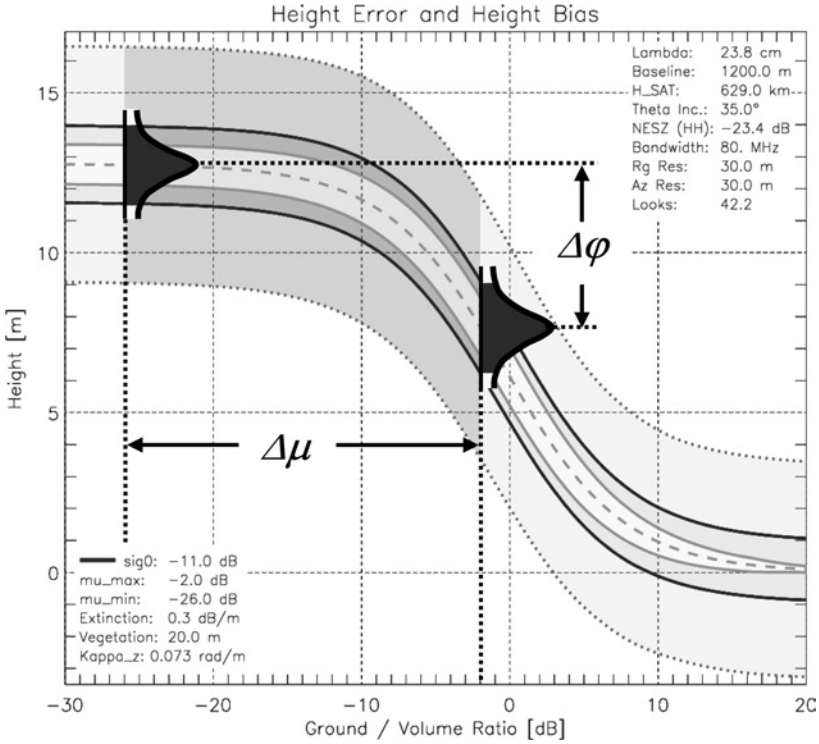

Fig. 7 *Vertical separation of interferometric phase centres ($\Delta\varphi$) in a TerraSAR-L single-pass interferometer as a function of the ground-to-volume scattering ratio μ*

which enables a measurement of the ground topography as well as a quantitative retrieval of important biophysical parameters such as vegetation height and density [82–85]. This is illustrated in Fig. 7, where the interferometric height errors are shown as a function of the ground-to-volume scattering ratio corresponding to different polarisations (cf. Krieger *et al.* [86]).

In this simulation, vegetation scattering has been approximated by the random volume over ground model, which combines the contributions from surface and volume scattering in a model comprising two vertical layers [82–85]. The grey dashed line in Fig. 7 illustrates the variation of the vertical phase centre as a function of the ground-to-volume scattering ratio for a vegetation layer with a height of 20 m and an extinction coefficient of 0.3 dB/m. The grey tube shows the height errors due to volume decorrelation for an effective baseline of 1200 m and an independent post-spacing of 30×30 m^2. The black tube shows additional height errors due to the limited system accuracy of the multistatic SAR polarimeter, assuming an illumination by TerraSAR-L. All errors are indicated as $\pm\sigma_h$ (standard deviation of the height errors) relative to the vertical phase centre. The darker areas of the tubes mark the expected range of ground-to-volume ratios ($\Delta\mu$) resulting from mapping a Scots Pine forest scenario with different polarisations at an incident angle of 35° [87]. The performance analysis predicts a sufficient separation ($\Delta\varphi$) of the vertical phase centres to enable a successful retrieval of the ground topography and important vegetation parameters such as volume height, extinction and so on. For comparison, the light black tubes show the expected height errors for a TerraSAR-L repeat-pass mission scenario with a temporal decorrelation of $\gamma_{temp} = 0.5$. In this case, there will be a significant overlap of the probability density functions at the left and right borders of the addressable ground-to-volume scattering range. Hence, a substantial performance gain can be expected by using a multistatic single-pass SAR interferometer instead of the conventional repeat-pass technique.

A configuration with three or more satellites is also of great advantage for polarimetric SAR interferometry, as multiple baselines allow for the more accurate inversion of scattering models, where the extinction coefficient varies as a function of volume height [85]. Multiple baseline interferometry has furthermore the potential to resolve phase ambiguities in areas with high vegetation and to solve problems from foreshortening (cf. Section 5). A further opportunity of a multistatic SAR interferometer is along-track interferometry (ATI), which compares the phase of two complex SAR images acquired in identical geometries but separated by a short time interval [88–94]. This technique is hence well suited for the monitoring of dynamic processes. Prominent applications of ATI are the measurement of ocean and tidal currents [88–90] and the detection and accurate velocity estimation of moving objects (Section 5). Large along-track baselines are required to detect objects with slow movement (e.g. ice drift), whereas short baselines are required to avoid ambiguities in the case of high velocities (e.g. traffic monitoring). Hence, an acquisition with multiple along-track baselines would be again of great help to resolve ambiguities, thereby enabling improved and more accurate velocity measurements [93, 94].

5 Multiple aperture sensing

A constellation of multiple radar satellites recording the scattered signals from a common illuminated footprint can be regarded as a large aperture system with sparsely distributed subaperture elements. The combination of multiple receiver signals can hence be treated in the framework of array processing. The opportunity to form very narrow antenna beams will, for example, allow for a space-variant suppression of range and azimuth ambiguities [95–97]. This will in turn lead to a reduction of the required antenna size for each receiver, thereby enabling cost-effective and powerful SAR missions with broad coverage and high resolution. One example for such a sparse aperture

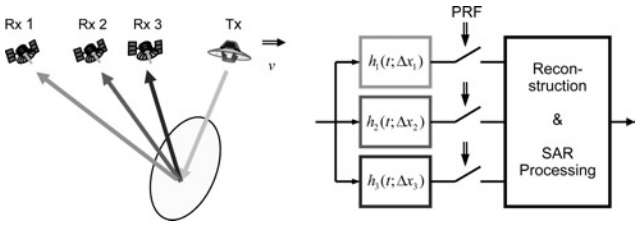

Fig. 8 *Multistatic sparse aperture SAR for high resolution wide-swath SAR imaging*

Left Satellite constellation
Right Linear system model

Table 2: System parameters of a distributed SAR for high resolution wide-swath imaging

Wavelength	24 cm
Antenna length (Tx)	5 m
Antenna length (Rx)	5 m
PRF	1350 Hz
Displacement (Rx 1)	400 m
Displacement (Rx 2)	800 m
Displacement (Rx 3)	1200 m
Slant range	800 km
Satellite velocity	7 km/s
Processed bandwidth	3750 Hz
SNR	20 dB

system is shown in Fig. 8 on the left, where a single transmitter (Tx) illuminates a wide image swath, and n passive receivers (Rx) record simultaneously the scattered signal from the illuminated footprint. Such a system is well suited to overcome the fundamental ambiguity limitation of conventional monostatic SAR systems where the unambiguous swath width and the achievable azimuth resolution pose contradicting requirements in the system design process. This becomes possible by a coherent combination of the individual receiver signals, which allows for a reduction of the pulse repetition frequency (PRF) by a factor of n without raising azimuth ambiguities [97]. The reduced azimuth sampling rate will then enable the mapping of a wide image swath with high azimuth resolution.

As an example, we consider an L-band system with three passive receivers (Table 2). Note that the short antennas enable an azimuth resolution of less than 3 m, whereas the low PRF of 1350 Hz allows for the unambiguous mapping of a wide image swath with a slant-range extension of ca. 100 km.

The data acquisition in such a multistatic SAR configuration can be described by a multichannel linear systems' model as shown in Fig. 8 on the right. On the basis of this model, a reconstruction algorithm has been derived, which allows for the recovery of the unambiguous SAR response from the highly ambiguous individual receiver outputs [97]. This is illustrated in Fig. 9. The left-hand side of Fig. 9 shows the processed azimuth response of a single receiver to a point scatterer located at an along-track position of 0 km. The response is highly ambiguous in azimuth with strong spurious responses at $x = k \cdot \mathrm{PRF} \cdot r_0 \cdot \lambda/(2v) = \{-37.0\ \mathrm{km}, -18.5\ \mathrm{km}, 18.5\ \mathrm{km}, 37.0\ \mathrm{km}\}$, which result from the short antenna length in combination with the low PRF. The right-hand side of Fig. 9 shows the reconstructed azimuth response after the coherent combination of the receiver signals. Note that in this simulation, the three receivers have a non-optimum, along-track displacement with slightly different Doppler centroids. Furthermore, independent white noise has been added to each receiver channel in order to simulate a more realistic scenario. It becomes clear that all ambiguities are well suppressed to a level below -20 dB in this example, which corresponds to the ambiguity level of a single satellite with a 3-fold PRF value (cf. third ambiguity in the left plot of Fig. 9).

The previous simulation illustrated the potential of a sparse satellite array for the unambiguous mapping of a wide image swath with high azimuth resolution. Note that the basic reconstruction algorithm in Krieger *et al.* [97] includes also the case of super-resolution in azimuth where multiple receivers record the scattered SAR signal with different Doppler centroids. This can be regarded as a band-pass decomposition of the SAR signal where each branch in the system model of Fig. 8 contains a narrow-band filter with no (or only partial) spectral overlap between adjacent channels. The achievable azimuth resolution is then given by the combined Doppler bandwidth from all receivers. The small Doppler bandwidth for each individual receiver requires, of course, more extended antennas than is required in the ambiguity suppression case. Both techniques can jointly be treated in the powerful framework of multichannel signal processing where they mark the extremes of a continuous range of potential multistatic system configurations for high resolution, wide-swath SAR imaging.

Sparse aperture systems enable also efficient clutter suppression for highly accurate velocity measurements of slowly moving objects on the ground and may overcome the problem of blindness against certain directions of

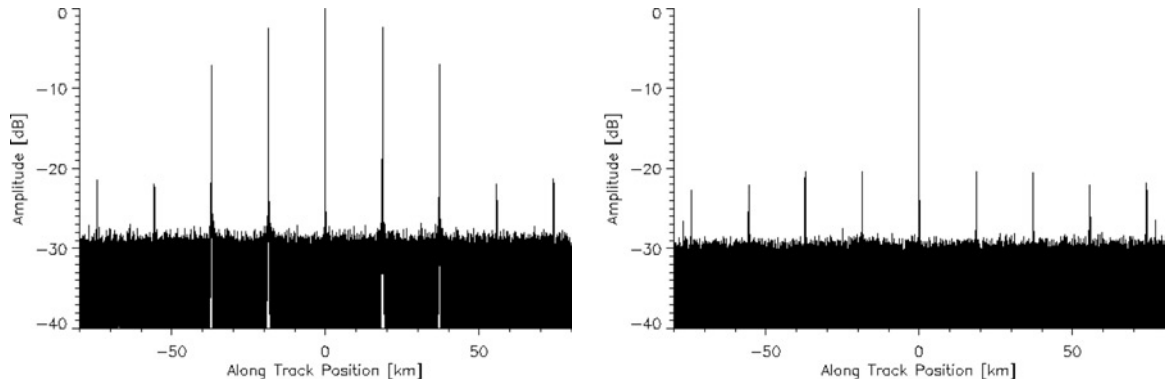

Fig. 9 *Reconstruction example for three receivers*

Left Response of one receiver
Right Sparse array response)

target motion [98–101]. Another opportunity is precise object localisation and tracking [8, 102]. A coherent combination of multiple SAR images acquired from slightly different incident angles can also improve the geometric and/or radiometric resolution [10, 103, 104]. The geometric super-resolution technique may again be regarded as the range-variant formation of narrow beams that divide each range resolution cell into smaller subcells with improved resolution. Super-resolution in range has furthermore the potential to overcome the bandwidth limitations for spaceborne SAR sensors posed by international frequency regulations. Another very promising application is SAR tomography [105–107], where several receivers are used to form a sparse aperture in the cross-track direction. This additional aperture enables a real 3D SAR imaging of semi-transparent volume scatterers. An important application is the mapping of vertical vegetation structures that enables global biomass estimates as required by the Kyoto protocol. A sparse aperture SAR with multiple cross-track baselines is also well suited to solve image distortions due to layover where spatially separated scatterers with different heights are mapped into the same resolution cell [108, 109]. Layover solution is also of high interest for interferometric DEM generation where it could enable data acquisitions with steep incident angles, thereby reducing potential data voids in mountainous terrain due to shadows.

6 Digital beamforming

Another promising technique for future bi- and multistatic SAR systems is digital beamforming on receive [110–114]. Consider as an example the geostationary illuminator concept (Section 2), where the antenna footprint of the transmitter exceeds by far the size of the receiver footprint. The small receiver footprint would hence limit the simultaneous data collection area. Such a waste of information (and energy) may be avoided by splitting the receiver antenna into multiple subapertures. As shown in Fig. 10 on the right, each subaperture signal is separately amplified, down converted and digitised. The digital signals are then combined in a dedicated processor to form multiple antenna beams with arbitrary shapes (Fig. 10, left). The opportunity to combine the recorded subaperture signals in many different ways introduces a high flexibility in operating the bistatic SAR constellation and makes effective use of the total signal energy in the large illuminated footprint.

Multiple beams in azimuth will allow for the division of a broad Doppler spectrum into multiple narrow-band subspectra with different Doppler centroids. The bandwidth in each subchannel corresponds to the total length of the receiver antenna, which determines the minimum PRF in the case of a single receiver (cf. Section 5 in the case of multiple receivers). A coherent combination of the subspectra will then yield a broad Doppler spectrum for high azimuth resolution. This technique is hence especially attractive for high resolution imaging with SAR systems that use long antennas for the unambiguous mapping of a wide swath. The formation of multiple beams in azimuth is also an interesting alternative to the displaced phase centre technique in Suess *et al.* [111]. Note that the suggested Doppler frequency splitting is functionally equivalent to the signal reception in a spotlight SAR where the beamsteering can be regarded as a temporal scanning of the different DBF channels in azimuth. The sensitivity of the whole system will therefore be comparable to a spotlight-on-receive SAR, whereas the final image has the highest azimuth resolution and, at the same time, spans the complete swath illuminated by the transmitter. The high azimuth resolution can also be used to improve the SNR or the radiometric resolution.

The formation of multiple independent beams in elevation allows for the simultaneous mapping of several distinct subswaths with high antenna gain. Each subswath can be mapped with a high PRF, which enables the use of short antennas to achieve high azimuth resolution. Residual range ambiguities could be suppressed by appropriate null-steering in elevation. Note that the spatial separation between the transmitter and receiver permits continuous recording, thereby avoiding possible gaps in the imaged swath (cf. Callaghan and Longstaff [115]). Finally, multiple subswaths will be combined to obtain wide coverage. The use of multiple antenna beams in elevation enables also an optimisation of the Rx antenna gain across the total image swath, thereby mitigating the common increase in the NESZ at the swath borders. Digital beamforming in elevation is hence well suited to reduce the antenna length on the cost of an increased antenna height. This supports the development of compact SAR sensors without the necessity of a complicated antenna folding during satellite launch.

Digital beamforming on receive allows also for a selective suppression of interferences. For example, the previously mentioned mapping of a wide image swath with multiple subswaths will require simultaneous transmission and reception to avoid gaps in the imaged swath. Interferences from nadir and/or direct transmit signals can then be suppressed by appropriate null-steering. A possible saturation of the low noise receiver amplifiers and/or subsequent A/D converters is avoided by using long transmit pulses or even frequency-modulated continuous wave illumination, which will also reduce the peak power requirements in the transmitter. A further potential of digital beamforming on receive is efficient endo-clutter suppression for

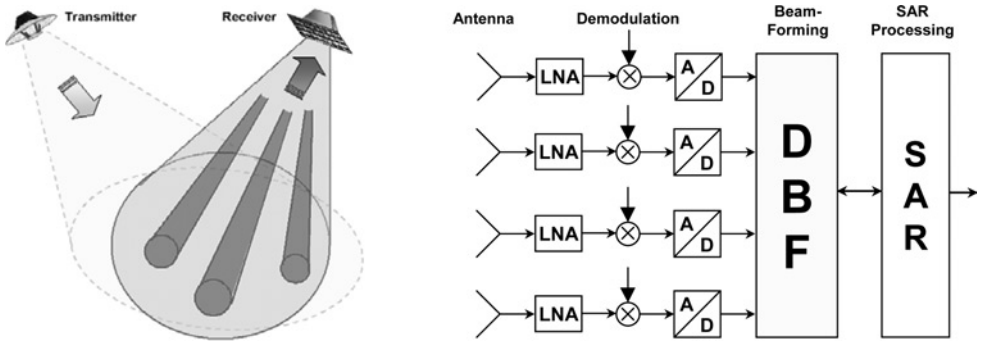

Fig. 10 *Bistatic SAR with digital beamforming on receive*

Left Illumination of a large footprint and reception of the scattered signals with multiple beams
Right Block diagram of digital beamforming on receive

reliable moving target indication (MTI). This becomes possible by a combined spatial and temporal processing of the recorded signals that allows for a directionally selective suppression of narrow Doppler frequency bands from stationary clutter [116]. Optimum processing schemes for MTI may be derived from the theory of space-time adaptive processing [117, 118]. This powerful technique allows also for the space-variant suppression of external interferences. All these modes can be implemented in a cost-efficient way by integrating receive-only modules with low power demands directly in the antenna. The above-mentioned techniques may also be combined with the interferometric (Section 4) and/or multiple array approach (Section 5) where a recording with multiple phase-centres helps to resolve residual ambiguities in the velocity estimation of moving objects [119]. Such a combination will be available with the TanDEM-X configuration, which provides four-phase centres on two different platforms [17].

7 Phase and time synchronisation

Oscillator stability is of special concern in bi- and multistatic SAR systems, as there is no cancellation of low-frequency phase errors as in a monostatic SAR, where the same oscillator signal is used for modulation and demodulation. Phase errors may cause a time-variant shift, spurious sidelobes and a widening of the impulse response, as well as phase errors in the focused SAR signal [120, 121]. Random-phase noise is often modelled by a second-order stationary stochastic process, which is conveniently characterised in the Fourier-frequency domain by its power spectral density $S_\varphi(f)$, where $S_\varphi(f)$ describes the one-sided spectral density of phase fluctuations in units of radians squared per hertz bandwidth at Fourier frequency f from the carrier [122, 123]. The left-hand side of Fig. 11 shows a typical phase spectrum $S_\varphi(f)$ of an ultra-stable local oscillator (USO) with a frequency of $f_{osc} = 10$ MHz. Simulation examples of the predicted bistatic phase errors in X-band are shown in the middle of Fig. 11 for a time interval of 50 s. Note that for better illustration, the contributions from a linear-phase ramp corresponding to different transmit and receive oscillator frequencies have been suppressed for each realisation of the stochastic process. A time series of focused azimuth responses is shown in Fig. 11 on the right for a coherent integration time of $T_A = 1$ s (no weighting has been used). It becomes evident that oscillator-phase noise may not only defocus the SAR image but it may also introduce significant distortions along the scene extension.

High-frequency phase noise will cause spurious sidelobes in the impulse response function. This deterioration can be characterised by the integrated sidelobe ratio (ISLR), which measures the transfer of signal energy from the mainlobe to the sidelobes. Note that because of the steep decay of the phase spectrum, high-frequency phase errors will mainly cause a transfer of the signal energy from the mainlobe to the first sidelobes (cf. simulation example given in Fig. 11). For an azimuth integration time T_A, the deterioration of the ISLR may be approximated from the phase spectrum as [1, 120, 124]

$$\mathrm{ISLR} \simeq \sigma_\varphi^2 = 2 \cdot \left(\frac{f_0}{f_{osc}}\right)^2 \cdot \int_{1/T_A}^{\infty} S_\varphi(f) \cdot \mathrm{d}f \qquad (8)$$

The factor 2 is due to the use of two independent oscillators and the scaling factor in the parentheses is due to the multiplication of the oscillator frequency f_{osc} by (f_0/f_{osc}) to obtain the radar signal with centre (carrier) frequency f_0. The upper integration limit may be substituted by the inverse of the transmit pulse duration, as higher frequency phase errors are averaged during range compression. The left plot of Fig. 12 shows estimates of the ISLR for the phase spectrum given in Fig. 11. A typical requirement for the maximum tolerable ISLR is -20 dB, which would, in this prototypical example, enable a coherent integration time T_A of 2 s in X-band. Such a prediction is also in good (qualitative) agreement with the results from several airborne bistatic radar experiments [124–128].

Quadratic phase errors will cause a widening of the azimuth response [120, 121]. For a bistatic SAR, these errors may be approximated by

$$\sigma_Q^2 = 2 \cdot \left(\frac{f_0}{f_{osc}}\right)^2 \cdot \frac{(\pi T_A)^4}{4} \cdot \int_0^{1/T_A} f^4 \cdot S_\varphi(f) \cdot \mathrm{d}f \qquad (9)$$

A typical requirement for quadratic phase errors is $\sigma_Q < \pi/2$, which would lead to a resolution loss of

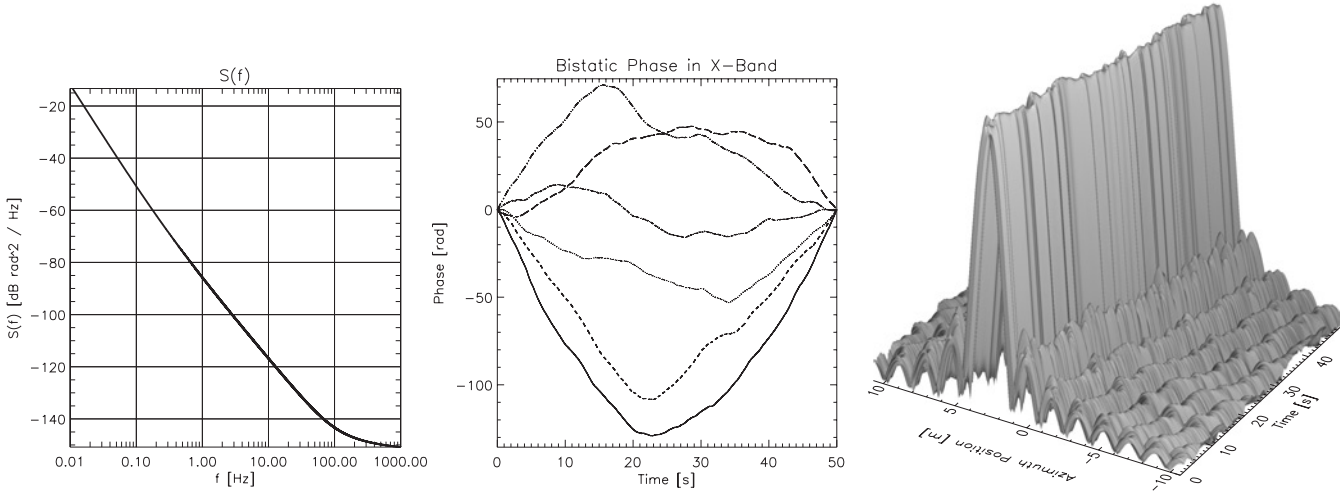

Fig. 11 *Modelling of bistatic phase errors by a stochastic process*

Left Power spectral density $S_\varphi(f)$ of oscillator phase noise (low-frequency values correspond to an Allan standard deviation [122] with $\sigma_a(\tau = 1\ \mathrm{s}) = 1 * 10^{-11}$, $\sigma_a(\tau = 10\ \mathrm{s}) = 2 * 10^{-11}$, $\sigma_a(\tau = 100\ \mathrm{s}) = 6 * 10^{-11}$)
Middle Example of quadratic and higher order bistatic phase errors in X-band for two independent oscillators (linear errors have been suppressed by subtracting appropriate phase ramps)
Right Focused azimuth response as a function of time ($T_A = 1$ s, $v_{sat} = 7$ km/s, $r_0 = 800$ km, $\lambda = 3.1$ cm)

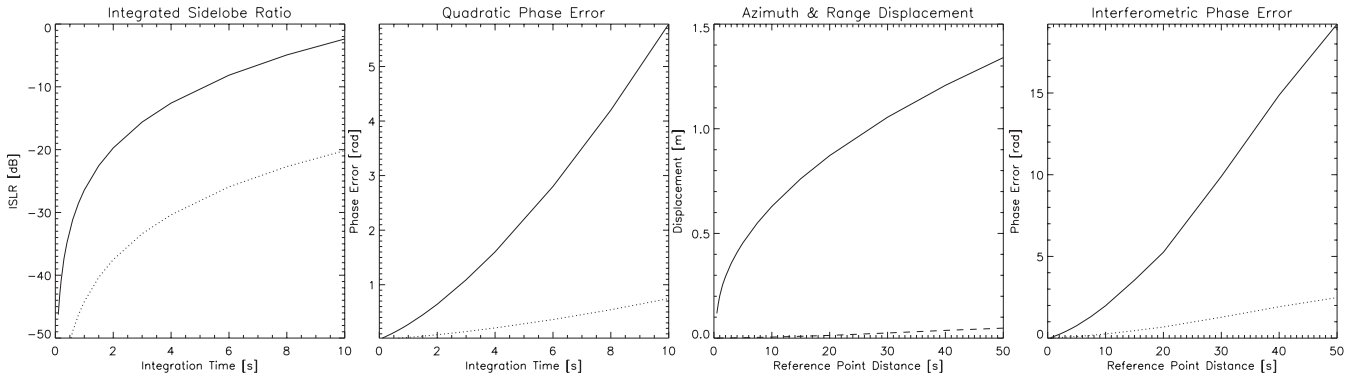

Fig. 12 *Impact of oscillator phase noise on the focusing of bistatic SAR images*

From left to right: ISLR; quadratic phase errors; azimuth (solid) and range (dashed) displacement; and interferometric phase error for X-band (solid) and L-band (dotted)

ca. 10% in the case of an unweighted azimuth processing [120]. The second plot in Fig. 12 shows estimates of the quadratic phase errors in X- and L-bands for the phase spectrum $S_\varphi(f)$ of Fig. 11. In this example, an integration time up to ca. 4 s would be allowed to ensure good bistatic focusing of the impulse response.

Any difference in the oscillator frequencies of the transmitter and receiver will cause a shift of the bistatic impulse response. For a non-squinted, quasi-monostatic imaging geometry, the azimuth shift is given by

$$\Delta x = \frac{c_0 r_0}{2 v_{\mathrm{sal}}} \cdot \frac{\Delta f}{f_{\mathrm{osc}}} \tag{10}$$

where v_{sat} is the satellite velocity, r_0 the slant range and $(\Delta f/f_{\mathrm{osc}})$ the relative frequency deviation between the two local oscillators. Note that a frequency deviation of only 1 Hz between two 10 MHz oscillators (corresponding to a relative frequency deviation of 10^{-7}) will cause a constant azimuth shift of $\Delta x = 1.7$ km for $v_{\mathrm{sat}} = 7$ km/s and $r_0 = 800$ km. This constant shift can be corrected for by ground control points or by an appropriate phase referencing system. The variance of the remaining azimuth shift may then be derived, from the spectral representation of the Allan variance with non-adjacent samples (cf. [123]), as

$$\sigma^2_{\Delta x}(t) = \left(\frac{c_0 r_0}{v_0}\right)^2 \cdot \int_0^\infty \frac{f^2}{f^2_{\mathrm{osc}}} \cdot S_\varphi(f) \cdot \left(\frac{\sin(\pi T_{\mathrm{A}} f)}{\pi T_{\mathrm{A}} f}\right)^2 \cdot \left[1 - \left(\frac{\sin(2\pi f t)}{2\sin(\pi f t)}\right)^2\right] \cdot \mathrm{d}f \tag{11}$$

where we assume a time interval t elapsed from the last reference point. The solid curve in the third plot of Fig. 12 shows the standard deviation of the predicted azimuth shift for the phase spectrum in Fig. 11 as a function of t. Note that the azimuth shift is independent of the wavelength. The range shift of the impulse response will be dominated by deviations between the transmitter and receiver PRFs. As the PRF is usually derived from the local oscillator by appropriate time division, the shift in slant range may be derived as

$$\Delta r(t) = \frac{c_0}{2} \cdot \left(\frac{1}{\mathrm{PRF}_{\mathrm{Rx}}} - \frac{1}{\mathrm{PRF}_{\mathrm{Rx}}}\right) \cdot t \cdot \mathrm{PRF}_{\mathrm{Tx}} \simeq \frac{c_0}{2} \cdot \frac{\Delta f}{f_{\mathrm{osc}}} \cdot t \tag{12}$$

where we assumed, for convenience, again a quasi-monostatic imaging geometry. A frequency deviation of 1 Hz between two 10 MHz oscillators will cause a linear range drift of the impulse response by 15 m/s. From this, it becomes clear that already small frequency deviations between the local oscillators may cause rather large range shifts during one scene acquisition. This may require a periodic PRF synchronisation to adapt the receiving window to the transmit event [125] or, as an alternative, continuous recording [10]. Furthermore, very precise time referencing will be required for precise range measurements. Possible solutions for time synchronisation in a bistatic radar are discussed in Weiß [129]. An alternative is the recourse to an appropriate set of calibration targets on the ground. The residual range shift Δr may then be estimated from

$$\Delta r = \frac{\lambda}{4\pi} \cdot \Delta\varphi \tag{13}$$

where $\Delta\varphi$ corresponds to the residual phase error not compensated by the periodic range calibration. For an estimate of $\Delta\varphi$, we assume the availability of a grid of (ground and/or phase reference) control points separated by a (temporal) distance of T_{C}. This will allow for the correction of low-frequency phase errors up to the frequency $1/(2T_{\mathrm{C}})$. (Note that in the case of a linear interpolation between the ground control points, the remaining interferometric phase errors would be more severe as can be gauged from the estimate of quadratic phase errors in (9) and Fig. 12.) Neglecting aliasing effects, the variance of the residual phase error may then be approximated by

$$\sigma^2_\varphi = 2 \cdot \left(\frac{f_0}{f_{\mathrm{osc}}}\right)^2 \cdot \int_{1/(2T_{\mathrm{C}})}^{1/T_{\mathrm{A}}} S_\varphi(f) \cdot \mathrm{d}f \tag{14}$$

The dashed line in the third plot of Fig. 12 shows the expected standard deviation of the residual range shift as a function of T_{C}.

Note that (14) describes also the residual interferometric phase errors after a correction of low-frequency phase errors up to the frequency $1/(2T_{\mathrm{C}})$. The right plot in Fig. 12 shows these remaining interferometric phase errors as a function of T_{C}. It becomes clear that the phase error will quickly increase with increasing control point separation T_{C}. This causes a low-frequency modulation of the interferometric phase, which affects mainly the absolute height error in the case of DEM generation. A special requirement for DEM generation is hence precise relative phase knowledge over long time intervals to avoid an excess of ground control points. Possible solutions are a direct exchange of radar pulses [17] or a ping-pong interferometric mode [9] in the case of fully active systems and an appropriate phase synchronisation link in the case of semi-active

constellations [130]. An alternative is the use of oscillators with significantly better long-term frequency stability. For example, the space qualified 5 MHz oscillators in Candelier *et al.* [131] have a short-term stability of $\sigma_a(\tau = 10\ \text{s}) = 10^{-13}$, which would decrease the interferometric phase errors in the right plot of Fig. 12 by two orders of magnitude. Note also that the requirements are significantly reduced for longer wavelengths.

8 Close formation flight and relative position sensing

Interferometric and sparse aperture sensing will require close satellite formations. Hence, orbit selection and collision avoidance may become a major design driver. For example, the satellite formation, shown in Fig. 6, would require a sufficient along-track separation between the receiver satellites to avoid a collision at the northern and southern turns. One possible solution is the use of an autonomous control system to ensure a minimum along-track displacement between the satellites [92]. An alternative is a slight modification of the orbit formation such that the orbits have an, additional vertical separation at the intersection of the orbital planes [132]. This can, for example, be achieved by a relative shift of the eccentricity vectors of the satellite orbits [71]. Fig. 13 illustrates this concept for the case of two satellites. The relative cross-track motion shown in Fig. 13 on the right can be regarded as forming a satellite HELIX, and such a formation will be used in the TanDEM-X mission [17]. The additional vertical (radial) separation between the satellites can be chosen rather small (e.g. $\sim$300 m) because a high momentum would be required to compensate this eccentricity-induced offset within a reasonable time span. The HELIX concept will hence enable a safe operation of the satellite formation, which is also of special interest in the case of contingency conditions. As there is no crossing of the satellite orbits in the HELIX configuration, the satellites may now be shifted arbitrarily along their individual orbits. This is of great advantage, as it enables almost vanishing along-track baselines for a given latitude range. Very short along-track baselines are, for example, desired in the case of DEM generation to avoid residual temporal decorrelation for some types of vegetation [133] or in the case of using the ocean surface for calibration purposes. The mapping of ocean currents will also require rather short along-track baselines to avoid ambiguities in the derivation of the velocity vector field [89, 90, 92]. The accurate control of the along-track displacement for a given orbit position requires precise actuation thrusters with very fine quantisation. An alternative is a controlled increase of the ballistic coefficient, for example, by appropriate satellite canting.

Many applications demand also very precise relative position sensing of the satellites. An example is cross-track interferometry where a relative 3D position sensing error of 1 cm may cause (in the worst case) an interferometric phase error of up to 116° in X-band and up to 15° in L-band. Baseline estimation errors will lead to a low-frequency modulation of the resulting interferogram that affects, in the case of DEM generation, mainly the absolute height accuracy while leaving the relative point-to-point height accuracy almost untouched. Very precise estimates of the relative satellite positions may be achieved by subtracting the received carrier phases from common GPS satellites. First investigations show that double difference carrier-phase differential GPS measurements enable an estimate of the interferometric baseline vector at the millimetre level in the case of close satellite formations [134, 135].

9 Bi- and multistatic processing

The focusing of bistatic SAR data will require robust and efficient processing algorithms. First promising steps in this direction have already been achieved [136–140]. Note that non-parallel satellite trajectories and/or different velocities may cause different range-Doppler histories for each point on the ground, thereby leading to a non-stationary data acquisition (cf. taxonomy in Ender *et al.* [128]). A simple example for such a shift-variant data acquisition is the geostationary illuminator concept given in Section 2, which violates the implicit assumption of translational invariance of many bistatic SAR processors. The processing of bistatic SAR data from airborne systems will furthermore require algorithms that enable an efficient incorporation of a bistatic motion compensation [126, 141].

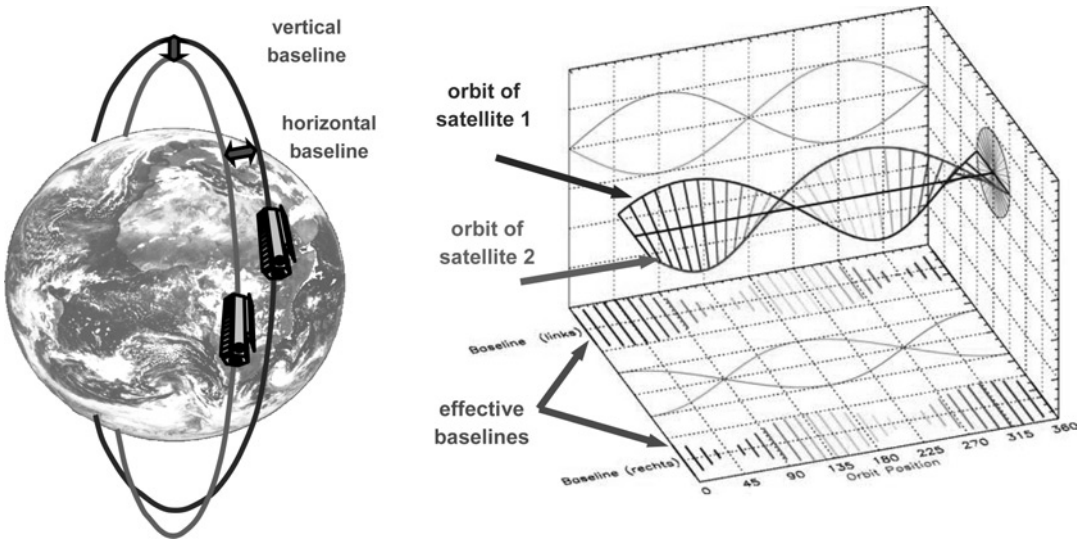

Fig. 13 *Eccentricity separation for TanDEM-X*

Left Orbital arrangement
Right Cross-track baselines as a function of the orbit position
The shown positions correspond to one complete orbit cycle (from Moreira *et al.* [132])

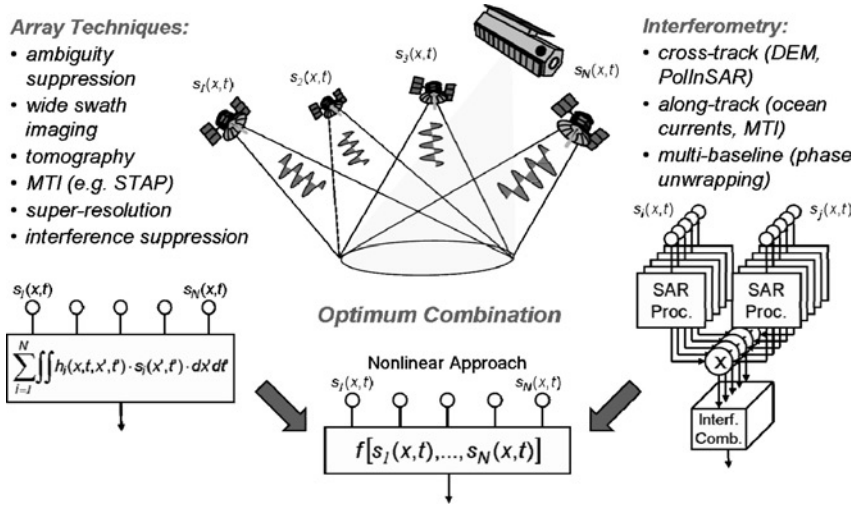

Fig. 14 *Combination of beamforming-like array processing techniques with the second-order interferometry in a unified processing framework*

The previous sections introduced several constellations of multiple radar satellites that simultaneously and coherently record the scattered signals from a common area on the Earth's surface. A combination of the recorded signals may be either linear like in 3D tomography, ambiguity suppression or super-resolution which are (essentially) based on a weighted superposition of the signals from the individual array elements (cf. Section 5), or nonlinear like in the various interferometric modes which evaluate the conjugate product of two or more SAR images (cf. Section 4). In order to take full advantage of the recorded data in a multistatic satellite configuration, it would be highly desirable to develop a generalised processing scheme that combines the various interferometric and array processing techniques in a unified framework (cf. Fig. 14). As an example, we consider the multistatic sparse aperture SAR for high-resolution wide-swath imaging in Fig. 8, where any cross-track separation of the receivers introduces topography-dependent phase offsets between the received signals. Successful ambiguity suppression will then require a compensation of these phase offsets, for example, via the simultaneous acquisition of a digital elevation model. This approach leads to a combination of linear along-track ambiguity suppression with the second-order cross-track interferometry, thereby enabling the use of small and cheap receiver satellites without an increase of the ambiguity level in case of multi-baseline DEM generation [24, 97].

A further challenge arises from the huge amount of data collected by multiple independent apertures. This will require broadband data links and/or appropriate data reduction strategies, for example, by an on-board pre-processing that exploits redundancies between the different channels. The redundancies could then be reduced by an appropriate bit-allocation in a 3D 'information cube', where the three axes correspond to time, frequency and spatial direction of the recorded signals, respectively. An optimised data compression may be derived from information theory by applying the general concept of rate distortion analysis to multichannel SAR systems [142]. Another possibility is the direct and selective parameter retrieval. This immediate and non-reversible data reduction would facilitate a data distribution directly to the users.

10 Conclusions

This paper has summarised new techniques and concepts towards a vision of a constellation of SAR satellites for global remote sensing. Several spaceborne bi- and multistatic SAR configurations have been introduced and their potentials and challenges for different applications such as frequent monitoring, wide-swath imaging, scene classification, cross-track interferometry and resolution enhancement are compared.

An example is the combination of a geostationary illuminator with multiple passive receivers in low Earth orbit (Section 2). Such a system is well suited to provide a cost-efficient solution to the frequent monitoring problem. A revisit time below 1 h can be achieved for the European continent with an appropriately designed constellation of ca. 30 small receiver satellites [33]. The constellation may furthermore be upgraded and/or reconfigured to a wealth of powerful remote-sensing modes such as along-track or cross-track interferometry, high-resolution wide-swath SAR imaging and even spaceborne tomography that enables a real 3D imaging of volume scatterers.

Bi- and multistatic SAR constellations have also the potential to make effective use of forward scattering, which may increase the SNR by 10 dB and more (Section 3). However, an established database for bistatic scattering of both natural scenes and artificial targets is not available yet. A bistatic SAR can furthermore provide a good ground resolution in all directions of the passive-receiver nadir, that is, high-resolution SAR imaging is also possible in the forward, downward and backward directions of the moving receiver (cf. Fig. 4). This property increases the access region and may also open new application areas such as a data fusion with simultaneously acquired data from different downward-looking sensors (e.g. optical, altimeter etc.) on the same platform. Another promising application of the bistatic SAR principle is a forward-looking imaging radar for airborne systems, where one or several stationary transmitters either in space or on the ground are combined with a passive SAR receiver on the aircraft. By this, a high image resolution may be achieved in the forward-looking direction without the necessity of a large cross-track antenna aperture [143, 144].

A powerful application of a multistatic radar is single-pass SAR interferometry (Section 4). The simultaneous data acquisition with multiple receivers eliminates major error sources such as atmospheric disturbances and temporal decorrelation, which put a strong limit on the achievable performance in conventional repeat-pass SAR interferometry. An ultimate performance may be achieved by the acquisition of multiple interferometric baselines in a single pass. Further potential for quantitative vegetation measurements arises from the use of fully polarimetric SAR configurations.

Multiple aperture sensing (Section 5) and digital beamforming on receive (Section 6) will make optimum use of the total signal energy in large illuminated footprints. For example, a combination of multiple aperture signals allows for the efficient suppression of ambiguities, which enables new SAR systems with wide coverage and high image resolution. This avoids conflicts from operating SAR systems in mutually exclusive imaging modes such as ScanSAR, Stripmap and Spotlight and enables regular observations of large areas, thereby satisfying a wider user community and facilitating mission planning. Further potential advantages are reliable MTI, efficient interference suppression, resolution enhancement and SAR tomography. High-power amplifiers are a prerequisite for wide-swath imaging with high geometric resolution. Sufficient signal energy may be provided by the use of conventional reflector antenna technology, thereby avoiding expensive Tx modules with lower efficiency.

Section 7 discussed the required phase accuracies for different bi- and multistatic SAR applications. We conclude that bistatic SAR focusing will be possible on the basis of appropriately selected USOs, whereas SAR interferometry is expected to require a phase synchronisation or a dense net of calibration targets. These requirements are somewhat relaxed for longer wavelengths. Furthermore, very accurate relative-position estimates of the satellites have to be available for interferometric applications such as DEM generation. Current investigations indicate an achievable baseline estimation accuracy in the millimetre range on the basis of a differential evaluation of GPS carrier phases (Section 8). The efficient focusing of bistatic SAR data requires new or modified processing algorithms. Several promising approaches have been suggested in the case of a translationally invariant satellite formation, but further developments are required for an efficient processing of the data from non-stationary data acquisitions (Section 9). The development of algorithms that combine the second-order interferometry with linear ambiguity suppression in a generalised nonlinear SAR processing framework remains a challenge. Further challenges arise from the calibration of bi- and multistatic SAR systems. For example, the joint antenna footprint in a bistatic SAR is given by the multiplication of two antenna patterns. Errors in the relative-antenna pointing may hence have a significant effect on the amplitude and the Doppler centroid of the recorded bistatic SAR signal.

One remaining factor for allowing the realisation and implementation of bi- and multistatic SAR configurations is the associated system costs. The possibility to distribute the required functionality on multiple satellites will have several advantages such as low-cost mass production due to the minimisation of recurrent costs, greater system reliability due to graceful degradation and lower launch costs by taking advantage of micro-satellite technology. A further aspect is the scalability by a phased deployment of the spacecraft. This allows for a distribution of the costs over a longer period of time, reduces the risk of a total mission failure and increases the flexibility by enabling a fast adaptation to changing threats or user requirements. A cost-benefit analysis has to take into account all these aspects when comparing single-satellite SAR missions with multifunctional satellite constellations. The new techniques and concepts summarised in this paper may be regarded as a first step in a paradigm shift from traditional LEO monostatic SAR systems towards highly reconfigurable satellite constellations for a broad range of powerful remote-sensing applications.

11 References

1 Willis, N.: 'Bistatic radar' (Artech House, Boston, 1991)
2 Skolnik, M.I.: 'Introduction to radar systems' (McGraw-Hill, New York, 1980)
3 Blake, L.V.: 'Radar range-performance analysis' (Lexington Books, MA, 1986)
4 Glaser, J.I.: 'Fifty years of bistatic and multistatic radar', *IEE Proc. F*, 1986, **133**, (7), pp. 596–603
5 Hartl, P., and Braun, H.M.: 'Bistatic radar in space', in 'Space based radar handbook' (Artech House, 1989)
6 Zebker, H., Farr, T., Salazar, R., and Dixon, T.: 'Mapping the world's topography using radar interferometry: the TOPSAT mission', *Proc. IEEE*, 1994, **82**, (12), pp. 1774–1786
7 Das, A., and Cobb, R.: 'TechSat 21 – space missions using collaborating constellations of satellites'. AFRL, Space Based Radar Workshop 1998, Atlanta, GA, USA, 1998
8 Martin, M., Klupar, P., Kilberg, S., and Winter, J.: 'Techsat 21 and revolutionizing space missions using microsatellites'. 15th Am. Inst. of Aeronaut. and Astronaut. Conf. on Small Satellites 2001, Utah, USA, 2001
9 Evans, N.B., Lee, P., and Girard, R.: 'The RADARSAT-2/3 topographic mission'. EUSAR 2002, Cologne, Germany, 2002, pp. 37–39
10 Massonnet, D.: 'Capabilities and limitations of the interferometric cartwheel', *IEEE Trans. Geosci. Remote Sens.*, 2001, **39**, (3), pp. 506–520
11 Moccia, A., Rufino, G., and D'Errico, M., *et al.*: 'BISSAT: a bistatic SAR for earth observation'. Phase A Study – Final Report, ASI Research contract I/R/213/00, 2001
12 Krieger, G., Fiedler, H., Mittermayer, J., Papathanassiou, K., and Moreira, A.: 'Analysis of multi-static configurations for spaceborne SAR interferometry', *IEE Proc., Radar Sonar Navig.*, 2003, **150**, (3), pp. 87–96
13 Underwood, C.I., Mitchell, O.S., and Jackson, C.: 'A novel method for achieving SAR imaging with a pair of micro-satellites by means of a bi-static configuration'. 16th Annual AIAA/USU Conf. on Small Satellites 2002, Logan, Utah, USA, 2002
14 Seguin, G., and Girard, R.: 'Interferometric missions using small SAT SAR satellites'. Pecora 15/ISPRS Conf. 2002, Denver, USA, 2002
15 Zink, M., Krieger, G., and Amiot, T.: 'Interferometric Performance of a Cartwheel Constellation for TerraSAR-L'. FRINGE Workshop 2003, Frascati, Italy, 2003
16 Runge, H., Gill, E., Eineder, M., and Suchandt, S.: 'An interferometric SAR satellite mission'. 54th Int. Astron. Congress 2003, Bremen, Germany, 2003
17 Moreira, A., Krieger, G., Hajnsek, I., Werner, M., Hounam, D., Riegger, S., and Settelmeyer, E.: 'TanDEM-X: a TerraSAR-X add-on satellite for single-pass SAR interferometry'. . IGARSS 2004, Anchorage, USA, 2004
18 Prati, C., Rocca, F., Giancola, D., and Monti Guarnieri, A.: 'Passive geosynchronous SAR system reusing backscattered digital audio broadcasting signals', *IEEE Trans. Geosci. Remote Sens.*, 1998, **36**, (6), pp. 1973–1976
19 Griffiths, H.D.: 'From a different perspective: principles, practice and potential of bistatic radar'. Proc. Int. Radar Conf. 2003, Adelaide, Australia, 2003, pp. 1–7
20 Cherniakov, M., Nezlin, D., and Kubik, K.: 'Air target detection via bistatic radar based on LEOS communication signals', *IEE Proc., Radar Sonar Navig.*, 2002, **149**, (1), pp. 33–38
21 Martin-Neira, M.: 'A passive reflectometry and interferometry system (PARIS): application to ocean altimetry', *ESA J.*, 1993, **17**, (4), pp. 331–355
22 Komjathy, A., Garrison, J., and Zavorotny, V.: 'GPS: A new tool for ocean science', *GPS World*, April 1999
23 Keydel, W.: 'Perspectives and visions for future SAR systems', *IEE Proc., Radar Sonar Navig.*, 2003, **150**, (3), pp. 97–103
24 Krieger, G., Fiedler, H., and Moreira, A.: 'Bi- and multistatic SAR: potentials and challenges'. Proc. EUSAR 2004, Ulm, Germany, 2004, pp. 365–369
25 Holt, B., and Hilland, J.: 'Rapid-repeat SAR imaging of the ocean surface: are daily observations possible?', *Johns Hopkins APL Tech. Dig.*, 2000, **21**, (1), pp. 7–14
26 International Ice Charting group: 'Ice information services: socio economic benefits and earth observation requirements.' Report to Group on Earth Observation and GMES, September 2004
27 Madsen, S., Chen, C., and Edelstein, W.: 'Radar options for global earthquake monitoring'. Proc. IGARSS 2002, Toronto, Canada, 2002
28 Fulghum, D., and Anselmo, J.: 'DARPA pitches small sats for tactical reconnaissance'. *Aviation Week Space Technol.*, 9 June 1997, pp. 29–31

29 Hsu, Y.S., and Loreti, D.C.: 'Spaceborne bistatic radar – an overview', *IEE Proc., Radar Sonar Navig.*, 1986, **133**, (7), pp. 642–648
30 Tomiyasu, K.: 'Bistatic synthetic aperture radar using two satellites'. IEEE EASCON, 1978, pp. 106–110
31 Hartl, P., and Braun, H.M.: 'A Bistatic Parasitical Radar (BIPAR)'. Proc. ISPRS, Kyoto, 1988
32 Sarabandi, K., Kellndorfer, J., and Pierce, L.: 'GLORIA: geostationary/low earth-orbiting radar image acquisition system: a multi-static GEO/LEO synthetic aperture radar satellite constellation for earth observation'. IGARSS 2003, Toulouse, France, 2003
33 Krieger, G., Fiedler, H., Hounam, D., and Moreira, A.: 'Analysis of system concepts for bi- and multistatic SAR missions'. IGARSS 2003, Toulouse, France, 2003
34 Moccia, A., Chiacchio, N., and Capone, A.: 'Spaceborne bistatic synthetic aperture radar for remote sensing applications', *Int. J. Remote Sens.*, 2000, **21**, (18), pp. 3395–3414
35 Eigel, R., Collins, P., Terzuoli, A., Nesti, G., and Fortuny, J.: 'Bistatic scattering characterization of complex objects', *IEEE Trans. Geosci. Remote Sens.*, 2000, **38**, (5), pp. 2078–2092
36 Burkholder, R.J., Gupta, I.J., and Johnson, J.T.: 'Comparison of monostatic and bistatic radar images', *IEEE Antennas Propag. Mag.*, 2003, **45**, (3), pp. 41–50
37 Gürel, L., Bagci, H., Castelli, J.C., Cheraly, A., and Tardivel, F.: 'Validation through comparison: measurement and calculation of the bistatic radar cross-section of a stealth target', *Radio Sci.*, 2003, **38**, (3), pp. 12-1–12-10
38 Mishra, A.K., and Mulgrew, B.: 'Ground target classification for airborne bistatic radar', 1st EMRS DTC Technical Conf., Edinburgh, 2004
39 Auterman, J.: 'Phase stability requirements for a bistatic SAR'. IEEE Nat. Radar Conf., Atlanta, USA, 1984, pp. 48–52
40 Dubois-Fernandez, P., Cantalloube, H., Vaizan, B., Krieger, G., Horn, R., Wendler, M., and Giroux, V.: 'ONERA-DLR SAR bistatic campaign: planning, data acquisition, and first analysis of bistatic scattering behaviour of natural and urban targets', *IEE Proc., Radar Sonar Navig.*, 2006, **153**, (3), pp. 214–223
41 Kell, R.E.: 'On the derivation of bistatic RCS from monostatic measurements', *Proc. IEEE*, 1965, **53**, (8), pp. 983–987
42 Ulaby, F.T., van Deventer, T.E., East, J.R., Haddock, T.F., and Coluzzi, M.E.: 'Millimeter-wave bistatic scattering from ground and vegetation targets', *IEEE Trans. Geosci. Remote Sens.*, 1988, **26**, (3), pp. 229–243
43 Hauck, B., Ulaby, F., and DeRoo, R.: 'Polarimetric bistatic-measurement facility for point and distributed targets', *IEEE Antennas Propag. Mag.*, 1998, **40**, (1), pp. 31–41
44 Nashashibi, A., and Ulaby, F.: 'Millimiter-wave polarimetric bistatic radar scattering from rough soil surfaces'. IGARSS 2003, Toulouse, France, 2003
45 Long, M.W.: 'Radar reflectivity of land and sea' (Artech House, 2001)
46 Domville, A.: 'The bistatic reflection from land and sea of X-band radio waves', GEC Electr: Ltd, Stanmore, England, Memorandum SLM 1802, 1967
47 Sarabandi, K., and Zahn, D.: 'Bistatic scattering measurements using near-field scanning'. IGARSS 2001, Sydney, Australia, 2001
48 Glaser, J.: 'Some results in the bistatic radar cross section (RCS) of complex objects', *Proc. IEEE*, 1989, **77**, pp. 639–648
49 Nashashibi, A., and Ulaby, F.: 'Detection of targets above rough surfaces using millimeter-wave bistatic radars'. IEEE APS Int. Symp., 2003, vol. 3, pp. 424–427
50 Farina, A.: 'Tracking function in bistatic and multistatic radar systems', *IEE Proc. F*, 1986, **133**, (7), pp. 630–637
51 Liang, P., and Pierce, L.: 'Application of bistatic MIMICS to forest canopies'. IGARSS 2004, Anchorage, USA, 2004
52 Ferrazzoli, P., Guerriero, L., and Solimini, D.: 'Could bistatic observations contribute to forest biomass monitoring'. IGARSS 2002, Toronto, Canada, 2002
53 Ferrazzoli, P., Guerriero, L., DelMonaco, C., and Solimini, D.: 'A further insight into the potential of bistatic SAR in monitoring the earth surface'. IGARSS 2003, Toulouse, France, 2003
54 Ceraldi, E., Franceschetti, G., Iodice, A., and Riccio, D.: 'Estimating the soil dielectric constant via scattering measurements along the specular direction', *IEEE Trans. Geosci. Remote Sens.*, 2005, **43**, (2), pp. 295–305
55 Peterson, A., Teague, C., and Tyler, G.: 'Bistatic radar observation of long-period, directional ocean-wave spectra with loran A', *Science*, 1970, **170**, pp. 158–161
56 Ruffini, G., Cardellach, E., Rius, A., and Aparicio, J.M.: 'Remote sensing of the ocean by bistatic radar observation: a review'. IEEC Report ESD-iom019-99, Barcelona, Spain, 1999
57 Fung, A., Zuffada, C., and Hsieh, C.Y.: 'Incoherent bistatic scattering from the sea surface at L-band', *IEEE Trans. Geosci. Remote Sens.*, 2001, **39**, (5), pp. 1006–1012
58 Elfouhaily, T., Thompson, D.R., and Linstrom, L.: 'Delay doppler analysis of bistatically reflected signals from the ocean surface: theory and application', *IEEE Trans. Geosci. Remote Sens.*, 2002, **40**, (3), pp. 560–573
59 Moccia, A., Rufino, G., and De Luca, M.: 'Oceanographic applications of spaceborne bistatic SAR'. Proc. IGARSS 2003, Toulouse, France, 2003
60 Barton, D.: 'Land clutter models for radar design and analysis', *Proc. IEEE*, 1985, **73**, (2), pp. 198–204
61 Ewell, G.W.: 'Bistatic radar cross section measurements', in Currie, N. (Ed.): 'Radar reflectivity measurement: techniques and applications' (Artech House, Norwood, 1989), Chap. 5
62 Khenchaf, A.: 'Bistatic scattering and depolarization by randomly rough surfaces: application to the natural rough surfaces in X-band', *Waves Random Med.*, 2001, **11**, pp. 61–89
63 Koudogbo, F., Mamesta, H.J., and Combes, P.F.: 'Surface and volume scattering from natural and manmade rough surfaces in the process of setting up data base coefficients'. IGARSS 2003, Toulouse, France, 2003
64 'Bistatic and multistatic radar (special issue)', *IEE Proc. F*, 1986, **133**, (7), pp. 585–668
65 Gens, R., and van Genderen, J.L.: 'SAR interferometry – issues, techniques, applications', *Int. Remote, J., Sens.*, 1996, **17**, (10), pp. 1803–1835
66 Bamler, R., and Hartl, P.: 'Synthetic aperture radar interferometry', *Inverse Probl.*, 1998, **14**, pp. 1–54
67 Madsen, S., and Zebker, H.A.: 'Imaging radar interferometry', in 'Principles and applications of imaging radar, manual of remote sensing' (John Wiley & Sons, 1998, Vol. 2), pp. 359–380
68 Massonnet, D., and Feigl, K.L.: 'Radar interferometry and its application to changes in the earth's surface', *Rev. Geophys.*, 1998, **36**, (4), pp. 441–500
69 Rosen, P.A., Hensley, S., Joughin, I.R., Li, F.K., Madsen, S.N., Rodriguez, E., and Goldstein, R.: 'Synthetic aperture radar interferometry', *Proc. IEEE*, 2000, **88**, (3), pp. 333–382
70 Hanssen, R.: 'Radar interferometry: data interpretation and error analysis' (Kluwer Academic Publishers, Dordrecht, 2001)
71 Fiedler, H., and Krieger, G.: 'Close formation of micro-satellites for SAR interferometry'. Proc. Formation Flying Symp. 2004, Washington, USA, 2004
72 Krieger, G., and Fiedler, H.: 'Definition of the TerraSAR-L cartwheel constellation: DEM performance estimation'. ESA-ESTEC Grant RFQ/3–10730/03/NL/CB, 2003
73 Eineder, M.: 'Problems and solutions for InSAR digital elevation model generation in mountainous terrain'. Proc. Fringe 2003 Workshop, Frascati, Italy, 2003
74 Ferretti, A., Monti Guarnieri, A., Prati, C., and Rocca, F.: 'Multibaseline interferometric techniques and applications'. Fringe 1996, Zurich, Switzerland, 1996
75 Massonnet, D., Vadon, H., and Rossi, M.: 'Reduction of the need for phase unwrapping in radar interferometry', *IEEE Trans. Geosci. Remote Sens.*, 1996, **32**, (2), pp. 489–497
76 Lombardini, F., and Griffiths, H.D.: 'Optimum and suboptimum estimator performance for multibaseline InSAR', *Frequenz*, 2001, **55**, pp. 114–118
77 Fornaro, G., and Monti Guarnieri, A.: 'Joint multibaseline SAR interferometry'. EUSAR 2004, pp. 333–336, Ulm, Germany, 2004
78 Eineder, M., and Adam, N.: 'Avoiding phase unwrapping in DEM generation by fusing multi frequency ascending and desecending interferograms'. IGARSS 2004, Anchorage, USA, 2004
79 Madsen, S., and Zebker, H.: 'Automated absolute phase retrieval in across-track interferometry'. Proc. IGARSS 1992, Houston, Texas, USA, 1992
80 Bamler, R., and Eineder, M.: 'Split Band Interferometry versus absolute ranging with wideband SAR systems'. IGARSS 2004, Anchorage, USA, 2004
81 Krieger, G., and Moreira, A.: 'Multistatic SAR satellite formations: potentials and challenges'. IGARSS 2005, Seoul, Korea, 2005
82 Cloude, S., and and Papathanassiou, K.: 'Polarimetric SAR interferometry', *IEEE Trans. Geosci Remote Sens.*, 1998, **36**, (5), pp. 1551–1565
83 Treuhaft, R.N., and Siqueira, P.R.: 'The vertical structure of vegetated land surfaces from interferometric and polarimetric radar', *Radio Sci.*, 2000, **35**, (1), pp. 141–177
84 Papathanassiou, K., and Cloude, S.: 'Single baseline polarimetric SAR interferometry', *IEEE Trans. Geosci. Remote Sens.*, 2001, **39**, (11), pp. 2352–2363
85 Cloude, S., and Papathanassiou, K.: 'Three-stage inversion process for polarimetric SAR interferometry', *IEE Proc., Radar Sonar Navig.*, 2003, **150**, (3), pp. 125–134
86 Krieger, G., Papathanassiou, K., and Cloude, S.: 'Spaceborne polarimetric SAR interferometry: performance analysis and mission concepts', *EURASIP J. Appl. Signal Process.*, 2005, **20**, pp. 3272–3292

87 Cloude, S., Corr, D., and Williams, M.: 'Target detection beneath foliage using polarimetric SAR interferometry', *Waves Random Med.*, 2004, **14**, (2), pp. 393–414
88 Goldstein, R.M., and Zebker, H.A.: 'Interferometric radar measurement of ocean surface currents', *Nature*, 1987, **328**, (20), pp. 707–709
89 Romeiser, R., Schwäbisch, M., Schulz-Stellenfleth, J., Thompson, D., Siegmund, R., Niedermeier, A., Alpers, W., and Lehner, S.: 'Study on concepts for radar interferometry from satellites for ocean (and Land) applications, 2002', www.ifm.uni-hamburg.de/~wwwrs/modeling/html/pro_kor.html
90 Romeiser, R.: 'On the suitability of a TerrSAR-L interferometric cartwheel for ocean current measurements'. IGARSS 2004, Anchorage, USA, 2004
91 Moccia, A., and Rufino, G.: 'Spaceborne along-track SAR interferometry: performance analysis and mission scenarios', *IEEE Trans. Aerosp. Electron. Syst.*, 2001, **37**, (1), pp. 199–213
92 Gill, E., and Runge, H.: 'A tight formation flight for along-track SAR interferometry'. Proc. Formation Flying Symp. 2004, Washington, USA, 2004
93 Carande, R.: 'Dual baseline and frequency along-track interferometry'. IGARSS 1992, Houston, Texas, USA, 1992
94 Lombardini, F., Bordoni, F., Gini, F., and Terrazzani, L.: 'Multibaseline ATI-SAR for robust ocean surface velocity estimation', *IEEE Trans. Aerosp. Electron. Syst.*, 2004, **40**, (2), pp. 417–433
95 Goodman, N.A., Lin, S.C., Rajakrishna, D., and Stiles, J.M.: 'Processing of multiple-receiver spaceborne arrays for wide area SAR', *IEEE Trans. Geosci. Remote Sens.*, 2002, **40**, (4), pp. 841–852
96 Aguttes, J.P.: 'The SAR train concept: required antenna area distributed over N smaller satellites, increase of performance by N'. IGARSS 2003, Toulouse, France, 2003
97 Krieger, G., Gebert, N., and Moreira, A.: 'Unambiguous SAR signal reconstruction from nonuniform displaced phase center sampling', *IEEE Geosci. Remote Sens. Lett.*, 2004, **1**, (4), pp. 260–264
98 Marais, K., and Sedwick, R.: 'Space based GMTI using scanned pattern interferometric radar'. IEEE Aerosp. Conf., Big Sky, MT, USA, 2001, vol. 4, pp. 2047–2055
99 Goodman, N.A., and Stiles, J.M.: 'A general signal processing algorithm for MTI with multiple receive apertures'. IEEE Radar Conf., Atlanta, 2004, pp. 315–320
100 Ender, J.H.: 'Spacebased SAR/MTI using multistatic satellite configurations'. EUSAR 2002, Cologne, Germany, 2002, pp. 337–340
101 Cerutti-Maori, D.: 'Performance analysis of multistatic configurations for spaceborne SAR/MTI based on the auxiliary beam approach'. EUSAR 2004, Ulm, Germany, 2004, pp. 631–634
102 Heimiller, R., Belyea, J., and Tomlinson, P.: 'Distributed array radar', *IEEE Trans. Aerosp. Electron. Syst.*, 1983, **19**, (6), pp. 831–839
103 Prati, C., and Rocca, F.: 'Improving slant-range resolution with multiple SAR surveys', *IEEE Trans. Aerosp. Electron. Syst.*, 1993, **29**, pp. 135–143
104 Gatelli, F., Monti Guarnieri, A., Parizzi, F., Pasquali, P., Prati, C., and Rocca, F.: 'The wavenumber shift in SAR interferometry', *IEEE Trans. Geosci. Remote Sens.*, 1994, **32**, (4), pp. 855–865
105 Reigber, A., and Moreira, A.: 'First demonstration of airborne SAR tomography using multibaseline L-band data', *IEEE Trans. Geosci. Remote Sens.*, 2000, **38**, (5), pp. 2142–2152
106 Rößing, L., and Ender, J.: 'Multi-antenna SAR tomography using superresolution techniques', *Frequenz*, 2001, **55**, pp. 123–128
107 Homer, J., Longstaff, I.D., She, Z., and Gray, D.: 'High resolution 3-D imaging via multi-pass SAR', *IEE Proc., Radar Sonar Navig.*, 2002, **149**, (1), pp. 45–50
108 Lombardini, F., Montanari, M., and Gini, F.: 'Reflectivity estimation for multibaseline interferometric radar imaging of layover extended sources', *IEEE Trans. Signal Process.*, 2003, **51**, (6), pp. 1508–1519
109 Gini, F., Lombardini, F., and Montanari, M.: 'Layover solution in multibaseline SAR interferometry', *IEEE Trans. Aerosp. Electron. Syst.*, 2002, **38**, (4), pp. 1344–1356
110 Steinberg, B., and Yadin, E.: 'Distributed airborne array concepts', *IEEE Trans. Aerosp. Electron. Syst.*, 1982, **18**, (2), pp. 219–227
111 Suess, M., Grafmüller, B., and Zahn, R.: 'A novel high resolution, wide swath SAR system'. IGARSS 2001, Sydney, Australia, 2001
112 Younis, M., Fischer, C., and Wiesbeck, W.: 'Digital beamforming in SAR systems', *IEEE Trans. Geosci. Remote Sens.*, 2003, **41**, (7), pp. 1735–1739
113 Krieger, G., and Moreira, A.: 'Potentials of digital beamforming in bi- and multistatic SAR'. IGARSS 2003, Toulouse, France, 2003
114 Moreira, A., and Krieger, G.: 'Synthetic aperture radar (SAR) systems: state of the art and future developments'. 33rd Eur. Microwave Conf. 2003, Munich, Germany, 2003, pp. 101–104
115 Callaghan, G.D., and Longstaff, I.D.: 'Wide swath spaceborne SAR using a quad element array', *IEE Proc., Radar Sonar Navig.*, 1999, **146**, (3), pp. 159–165
116 Ender, J.: 'Space-time processing for multichannel synthetic aperture radar', *Electron. Commun. Eng. J.*, 1999, **11**, (1), pp. 29–38
117 Klemm, R.: 'Principles of space time adaptive processing' (IEE, London, 2002)
118 Klemm, R. (Ed.) 'Applications of space-time adaptive processing' (IEE, London, 2004)
119 Friedlander, B., and Porat, B.: 'VSAR: a high resolution radar system for ocean imaging', *IEEE Trans. Aerosp. Electron Syst.*, 1998, **34**, (3), pp. 755–775
120 Buckreuss, S.: *Bewegungskompensation für flugzeuggetragene SAR systeme*' (DLR Forschungsbericht 94–17, 1994), (see also: Buckreuss, S., 'Motion errors in an airborne synthetic aperture radar system', *ETT-J.*, 1991, **2**(6), pp. 55–64)
121 Hounam, D., Panula-Otto, E., and Wägel, K.: 'Oscillator noise and SAR image quality' (DLR Forschungsbericht, 1994)
122 Rutman, J.: 'Characterization of phase and frequency instabilities in precision frequency sources: fifteen years of progress', *Proc. IEEE*, 1978, **66**, (9), pp. 1048–1073
123 Barnes, J.A., Chi, A.R., and Cutler, L.S., *et al*.: 'Characterization of frequency stability', *IEEE Trans. Instrum. Meas.*, 1971, **20**, (2), pp. 105–120
124 Auterman, J.L.: 'Phase stability requirements for a bistatic SAR'. Proc. IEEE Natl. Radar Conf., Atlanta, USA, 1984, pp. 48–52
125 Wendler, M., Krieger, G., and Horn, R., *et al*.: 'Results of a bistatic airborne SAR experiment'. Proc. Int. Radar Symp. 2003, Dresden, Germany, Sponsored by DGON, 2003, pp. 247–253
126 Cantalloube, H., Wendler, M., Giroux, V., Dubois Fernandez, P., and Krieger, G.: 'Challenges in SAR processing for airborne bistatic acquisitions'. EUSAR 2004, Ulm, Germany, 2004, pp. 577–580
127 Yates, G., Horne, A.M., Blake, A.P., Middleton, R., and Andre, D.B.: 'Bistatic SAR image formation'. EUSAR 2004, Ulm, Germany, 2004, pp. 581–584
128 Ender, J., Walterscheid, I., and Brenner, A.: 'New aspects of bistatic SAR: processing and experiments'. IGARSS 2004, Anchorage, USA, 2004
129 Weiß, M.: 'Synchronisation of bistatic radar systems'. IGARSS 2004, Anchorage, USA, 2004
130 Eineder, M.: 'Oscillator clock drift compensation in bistatic interferometric SAR'. Proc. IGARSS 2003, Toulouse, France, 2003
131 Candelier, V., Canzian, P., Lamboley, J., Brunet, M., and Santarelli, G.: 'Space qualified 5 MHz ultra stable oscillators'. Int. Frequency Control Symp. 2003, Tampa, FL, USA, 2003, pp. 575–582
132 Moreira, A., Krieger, G., and Mittermayer, J.: 'Comparison of several bi-static SAR configurations for spaceborne SAR interferometry'. Proc. ASAR Workshop 2001 (see also US Patent No. 6,677,844 B2, 2002), 2001
133 Narayanan, R.M., Doerr, D.W., and Rundquist, D.C.: 'Temporal decorrelation of X-band backscatter from wind-influenced vegetation', *IEEE Trans. Aerosp. Electron. Syst.*, 1992, **28**, (2), pp. 404–412
134 Flechtner, F.: 'Relative baseline determination for a tandem SAR mission using GPS code and phase measurements.'. GFZ (Geo-Forschungs-Zentrum Postsdam), Technical Note, August 2003
135 Kroes, R., and Montenbruck, O.: 'Spacecraft formation flying: relative positioning using dual-frequency carrier phase', *GPS World*, July 2003, pp. 37–42
136 Soumekh, M.: 'Bistatic synthetic aperture radar inversion with application in dynamic object mapping', *IEEE Trans. Signal Process.*, 1991, **39**, (9), pp. 2044–2055
137 Ding, Y., and Munson, D.: 'Fast back projection algorithm for bistatic SAR imaging'. IEEE Int. Conf. on Image Processing 2002, Rochester, 2002
138 Aria, D., Monti Guarnieri, A., and Rocca, F.: 'Focusing bistatic synthetic aperture radar using dip move out', *IEEE Trans. Geosci. Remote Sens.*, 2004, **42**, (7), pp. 1362–1376
139 Loffeld, O., Nies, H., Peters, V., and Knedlik, S.: 'Models and useful relations for bistatic SAR processing', *IEEE Trans. Geosci. Remote Sens.*, 2004, **42**, (10), pp. 2031–2038
140 Neo, Y., Wong, F., and Cumming, I.: 'Focusing bistatic SAR images using nonlinear chirp scaling'. Radar 2004, Toulouse, France, 2004
141 Kirk, J.C.: 'Bistatic SAR motion compensation'. IEEE Int. Radar Conf. 1985, Arlington, VA, USA, 1985, pp. 360–365
142 Berger, T.: 'Rate Distortion Theory' (Prentice Hall, Englewood Cliffs, NJ, 1971)
143 Krieger, G., Mittermayer, J., Buckreuss, S., Wendler, M., Sutor, T., Witte, F., and Moreira, A.: 'Sector imaging radar for enhanced vision', *Aerosp. Sci. Technol.*, 2003, **7**, pp. 147–158
144 Wirth, W.-D.: 'Radar techniques using array antennas' (IEE, London, 2001)
145 Simpson, R.A.: 'Spacecraft studies of planetary surfaces using bistatic radar', *IEEE Trans. Geosci. Remote Sens.*, 1993, **31**, (2), pp. 465–482